Accepted Manuscript

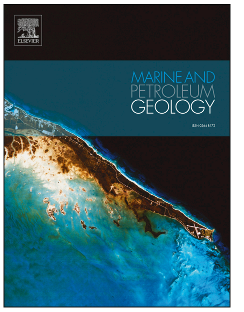

Sea floor bedforms and their influence on slope accommodation

V. Maselli, B. Kneller, O.L. Taiwo, D. Iacopini

PII: S0264-8172(19)30024-8

DOI: https://doi.org/10.1016/j.marpetgeo.2019.01.021

Reference: JMPG 3690

To appear in: *Marine and Petroleum Geology*

Received Date: 22 October 2018

Revised Date: 16 January 2019

Accepted Date: 21 January 2019

Please cite this article as: Maselli, V., Kneller, B., Taiwo, O.L., Iacopini, D., Sea floor bedforms and their influence on slope accommodation, *Marine and Petroleum Geology* (2019), doi: https://doi.org/10.1016/j.marpetgeo.2019.01.021.

Title: Sea floor bedforms and their influence on slope accommodation.

Authors: Maselli, V.[1,2], Kneller, B.[2], Taiwo, O.L.[2], Iacopini, D.[2]

[1]Department of Earth Sciences, Life Sciences Centre, Dalhousie University, 1355 Oxford Street, Halifax, Nova Scotia, B3H 4R2, Canada.

[2]School of Geosciences, University of Aberdeen, Meston Bld., King's College, Aberdeen, AB24 3UF, United Kingdom.

Keywords: Stoss-side accommodation, ponded lobes, turbidity currents, bedforms, offshore Brazil.

Highlights:

1- This study focuses on the continental slope of the Potiguar Basin, offshore Brazil.

2- 3D seismic data reveal large- and short-wavelength bedforms.

3- Coarse-grained ponded lobes accumulate on the stoss side of the large-wavelength bedforms.

4- The concept of stoss-side accommodation is introduced.

Abstract

In deep-water settings, the accommodation for sediment transported by turbidity flows relates to the difference between the elevation of the depositional surface and its equilibrium profile. As a consequence, accommodation creation, or disruption, may depend from changes in the physiography of the receiving basin, or changes in the flow properties. In topographically complex slopes, such where salt-withdrawal intra-slope basins occur, three different types of accommodation have been recognized. Among other parameters, the ratio between flow

thickness and depth of the intra-slope basin controls the partial, or full, ponding of the sediment in suspension, and consequently, the lithology distribution within the deposit. On a smaller spatial scale, the behavior of bottom-hugging sediment-laden flows can be affected by topographic variations of the sea floor associated with the presence of km-scale bedforms. In this work, we show that ponded lobes accumulate on the convex-up stoss side of pre-existing large-wavelength bedforms (length up to 10^3, and height up to 10^2), and that their lithology distribution depends on the flow characteristics respect to the bedform height. In detail, when partial ponding of turbidity currents occurs, flow stripping promotes the accumulation of the coarse-grained fractions on the stoss side of the bedform, while the fine-grained cloud over-spills the lee side, affecting deposition basinward. By introducing the concept of *stoss-side accommodation*, this work suggests a new mechanism for the formation of ponded coarse-grained facies in slope settings due to the trapping effect large-wavelength bedforms with convex-up stoss sides.

1. Introduction

Accommodation (or accommodation space) was defined by Vail (1987) and Jervey (1988) as the space available for sediment accumulation, with global sea level change and tectonic processes (driving subsidence or uplift of the sea floor) considered as first order controls. In shallow water shelfal systems, the accommodation available is also dependent on the energy of marine processes, such as waves, longshore drift or tides, and by the presence of topographic lows, such as incised valleys (Dalrymple et al., 1992). In deep-water settings, the concept of accommodation was expanded considering the analogy between subaerial (rivers) and submarine channels, both characterized by downstream concave-up equilibrium profiles and a base level (Carter, 1988; Prather et al., 1998; Pirmez et al., 2000; Kneller, 2003; Ferry et al., 2005).

A topographic profile is considered in equilibrium, or at grade, when the kinetic energy distribution along the system is such that no net sediment aggradation or erosion occurs. In fluvio-deltaic systems, the base level coincides with sea or lake levels (i.e. the river mouth), while for submarine channels the base level was defined as the deepest point reached by a gravity-driven flow (Carter, 1988), or the point where the transition from confined to unconfined flow occurs (Kneller, 2003). Turbidity currents exert a paramount control on the shape of the equilibrium profile with the gradient of submarine channels directly related to the flow conditions (flow density, thickness, grain size, mud content; Mutti et al., 1999; Kneller, 2003). Considering the above, the accommodation was defined by the difference between the topography of the depositional surface (i.e., the thalweg of a slope turbidite channel) and its equilibrium profile (Prather et al., 1998; Pirmez et al., 2000). When a submarine channel is at grade, the accommodation is limited, a meandering planform morphology develops, with no aggradation or incision (Kneller, 2003), producing fluvial-like meander belts (Abreu et al., 2003; McHargue et al., 2011; Kolla et al., 2012). A disequilibrium between the channel thalweg and the graded profile will lead to accommodation creation or destruction that the system will exploit through deposition within the channel or erosion of its thalweg and rejuvenation of the system (Pirmez et al., 2000; Heiniö and Davies, 2007). Several mechanisms, mainly driven by tectonic processes (Prather et al., 1998; Pirmez et al., 2000; Ferry et al., 2005) or emplacement of mass-transport deposits (Armitage et al., 2009; Kneller et al., 2016 and references therein), may lead to the formation of accommodation for sediment deposition. The topography of the slope may change in response to shale or salt diapirism under loading by thick sediment accumulations, or in response to gravitational tectonics driven by rapid sedimentation along passive margins (Prather, 2003), or by crustal extension or compression, leading to the formation of ponded and healed-slope accommodation space (*sensu* Prather et al., 1998). Ponded slope basins have been recognized in different settings, both modern and ancient, and extensively investigated in the Gulf of Mexico and in the Eastern Equatorial Atlantic margin (Prather et al., 1998; Beaubouef and Friedmann, 2000; Badalini et al., 2000; Pirmez et al., 2000; Sinclair and Tomasso, 2002; Booth et al., 2003; Smith, 2004; Adeogba et al., 2005; Barton, 2012; Deptuck et al., 2012; Prather et al., 2012; Jobe et al., 2015; Jobe et al., 2017; Hawie et al., 2018). Through integration of seismic and well data, the motif of the sedimentary infill has been interpreted in terms of a process of fill-and-spill, i.e. filling of the mini-basin by ponded turbidites and associated deposits, and subsequent bypass from the shallower mini-basin to the one downslope (Winker, 1996; Prather et al., 1998; Badalini et al., 2000; Prather et al., 2012). Mass-transport deposits (MTDs), ubiquitously recognized in all margin settings (Moscardelli and Wood, 2016), have the potential to generate different styles of accommodation and to control deep-water sediment routing systems (Kneller et al., 2016; Soutter et al., 2018). Sediment may accumulate along the evacuation zone of submarine landslides or along the relative topographic lows generated atop the MTDs by the presence of blocks, faults, folds and compaction (Kneller et al., 2016; Ward et al., 2018).

Local topographic changes of the sea floor (i.e., bedforms) have been observed on the slope in association with the passage of gravity-driven flows such as turbidity currents, or of bottom currents (Wynn and Stow, 2002; Smith et al., 2007; Piper and Normark, 2009; Rebesco et al., 2014; Talling et al., 2015; Symons et al., 2016 and references therein). Turbidity and bottom currents interacting with the sea floor may generate depositional (sediment waves), erosional (scours), or mixed bedforms (terminology *sensu* Symons et al., 2016). Bedforms of different shapes, aspect ratio, direction of migration and grain size, from mud to gravel, have been recognized in both confined and unconfined settings, such as shelfal systems (Berndt et al., 2006), pro-delta slopes (Casalbore et al., 2017), channel axis (Paull et al., 2010; 2011), channel levees (Normark et al., 2002), and channel-lobe transitions (Carvajal et al., 2017).

After the seminal work of Fildani et al. (2006) on the Monterey East Channel, increasing attention has been dedicated to the study of supercritical bedforms. Cyclic steps and antidunes have been recognized along delta fronts (Normandeau et al., 2016; Hughes Clarke, 2016; Kostic et al., 2019) and slope channel systems (Covault et al., 2017), and a growing body of evidence has suggested that channels may evolve from a series of erosional bedforms arranged in a cyclic manner (i.e., cyclic steps; Fildani et al., 2013; Covault et al., 2014). On the sea floor, erosional bedforms, or those with an erosional component, may reach in excess of 10^3 m in length and width, and up to 10^2 m in height (Cartigny et al., 2011; Symons et al., 2016), often showing circular to elliptical morphology, such as in the case of the Monterey East channel (Fildani et al., 2006). With respect to the adjacent sea floor, the stoss side of such bedforms may constitute an area of lower bathymetry, consequently generating accommodation for sediment accumulation.

This study aims to understand how sea floor bedforms may generate slope accommodation, and may promote deposition from bottom-hugging sediment-laden flows. In detail, using an example from the Brazilian slope, we discuss how the convex-up stoss side of large-wavelength bedforms (up to 4 km in length, and 150 m in height) may trap the sediment transported by turbidity currents, and how the 3D topography of the sea floor may promote transformation of the flow.

2. Study Area and Geological Setting

The present study focuses on a portion of the Brazilian slope just south of the Equator, in the offshore Potiguar Basin, in water depths between ca. 700 m and 1800 meters below mean sea level (m bmsl; Fig. 1). The area is characterized by a ca. 60 km wide, low angle (0.04°), shelf, and a steep slope, dipping towards NE at ca. 3.8°. Towards the basin, a series of volcanic islands and structural highs is present, creating troughs that interrupt the continuity of the slope (Fig. 1).

The Potiguar Basin is a NE-trending aborted rift with ~6,000 m thick sedimentary infill, structurally characterized by SW-NE-trending asymmetric grabens separated by internal basement horsts (Matos, 2000; Jovane et al., 2016). The rifting process began in response to continental breakup between the Borborema and Benin-Nigeria provinces during the South Atlantic opening in the Early Cretaceous (Matos, 2000). Rift phase deposition during the Aptian to Campanian, consisted of fluvial to shallow-marine transgressive sediments (Araripe and Feijó, 1994). The drift phase, starting in the Campanian, is characterized by thermal subsidence and deposition of fluvio-deltaic to deep-water clastic sediments, with the Cenozoic mainly recording the onset and evolution of the submarine canyon systems still active today.

3. Data and Methods

The dataset from the Potiguar Basin used in the present study consists of a high-quality 3D full stack, Kirchhoff time-migrated reflection seismic volume, covering about ~2000 km^2, and acquired by PGS in 2009 (Fig. 1). The line spacing is 12.5 m in both in-line and cross-line directions, which are oriented NW-SE and SW-NE, respectively. The sampling interval is 2 milliseconds (ms). The data are zero-phase migrated and displayed with Society for Exploration Geologists (SEG) normal polarity, so that an increase in acoustic impedance is represented by a blue-red-blue loop, while a decreasing acoustic impedance is shown as a red-blue-red loop. The dominant frequency (F) of the section of interest (upper 250 ms below the seabed) ranges between 40 and 75 Hz. Sound velocities of 1,500 ms^{-1} and 1,800-2,500 ms^{-1} have been respectively assigned for sea water and for the investigated interval below the sea floor, with the latter velocity obtained from the sonic log of well CES-112, located 2 km to the SE (see Fig. 1; Conde et al., 2007). Using those end-member velocities and frequencies, we estimate a vertical resolution (defined as tuning thickness) as 5 m at the sea floor and 6 to 15.5 m for the units below. Taking into account the focusing effect of Kirchhoff migration (Brown, 2004), the horizontal resolution can be considered equivaled to the line spacing, i.e. 12.5 m. However, our ability to recognize sea floor features in plan view, defined as detectability or limit of visibility (Brown, 2004), can go below the tuning thickness limit (Reijenstein et al., 2011). Thus, we can describe geological and sedimentary features or patterns smaller than the tuning thickness, although our capacity to define volumes is limited by the tuning thickness.

The bathymetry of the sea floor, presented at 12.5 × 12.5 m horizontal resolution (Fig. 2), was generated picking the first reflection from the 3D seismic data. Two other seismic horizons, H1 and H2, were identified on 2D arbitrary lines extracted from the 3D seismic volume, based on the seismic facies and reflector terminations. The structural map of each seismic horizon is presented as a surface gridded at 12.5 × 12.5 m horizontal resolution.

Seismic attributes have been calculated and extracted from the sea floor horizon and include both amplitude-derived (root-mean-square, RMS) and time-derived (variance) values. While the variance, which measures the similarity of consecutive waveforms over a given sampling window (3 × 3 traces in the present study), is useful for imaging lateral discontinuities (Bahorich and Farmer, 1995; Chen and Sidney, 1997; Brown, 2004), the RMS amplitude, which represents the square root of the arithmetic mean of the squares of the amplitudes within a defined window interval (3 instantaneous traces in the present study), is helpful for revealing coarse-grained facies (Rijks and Jauffred, 1991; Chen and Sidney, 1997; Brown, 2004).

4. Results

4.1. Sea floor morphology

The sea floor shows two main canyon systems, named C-1 and C-3 that are located towards NW and SE corners of the dataset, respectively (Fig. 2). The depth of both canyons changes from ca. 400 m to less than 200 downslope, while the thalweg presents an average gradient of 2.7° and a sinuosity index of 1.158, for C-1, and a gradient of 3.8° and a sinuosity index of 1.028, for C-3 (Fig. 2). A smaller channel, C-2, ca. 90 m deep, crosses the slope with an average thalweg gradient of 4.15° and a sinuosity index of 1.031. The present study focuses on the slope area between C-2 and C-3 (confined by the red line in Fig. 2).

Two narrow channel incisions (named C-A and C-B, Fig. 2), up to 60 m deep and oriented SW-NE, form upstream of a topographic step (slope break) oriented approximately NS (dashed red line in Fig. 2). Farther downslope, the sea floor presents a series of large-wavelength bedforms (Fig. 3), named LB1 to LB4, which are clearly highlighted by the variance attribute extracted from the sea floor horizon (Figs. 3 and 4). The bedform wavelength changes from ca. 4 km (LB1, Fig. 5) to less than 1 km (LB4, Fig. 5), while the bedform height from ca. 150 m (LB1, Fig. 5) to less than 50 m (LB4, Fig. 5). The crests of the bedforms show a sinuous shape, with dominant downslope convexity (Fig. 3), and are progressively shifted towards the east moving downdip, following the maximum gradient of the sea floor. In cross section on the sea floor, the bedforms are downslope asymmetric, with seaward dipping (LB1 and LB2, Fig. 3 bottom) or sub-horizontal (LB3 and LB4) stoss sides, and up to 8° dipping lee sides. A series of small channels (named gutter-like channels) cut the lee sides of LB1 to LB4 with up to 15 m deep incisions (Fig. 4), and the slope on the east side of C-2 (Figs. 3, 4). Shallower and narrower incisions are also present on the stoss side of LB1 (Figs. 3, 4).

Two fields of short-wavelength bedforms can be detected on the sea floor downdip of the slope break at the mouths of C-A and C-B (SB1a on the stoss side of LB1, and SB1b, Fig. 3). The bedforms are both symmetric (section a-b in Fig. 6) and asymmetric (section c-d in Fig. 6), with sinuous crests (Fig. 6, right). Wavelengths and heights are, on average, 120 m and 8 m, respectively (Fig. 5). A third train of bedforms (named SB2) with linear crests and ca. 5 m wave heights is present on the lee side of LB3 (SB2 in Fig. 3; section e-f in Fig. 6). We are confident that the spatial (vertical and horizontal) resolution of the sea floor generated by picking the sea floor horizon on the 3D seismic dataset is high enough to visualize such small-scale sea floor features. Seismic artefacts are present in the data, as indicated the contour-parallel undulations highlighted by the slope map of Fig. 6, but they are characterized by a totally different seismic footprint (see section g-h in Fig. 6), unrelated to the bathymetry, with wave height and length extremely short, which will not have any effect on the interpreted structures.

The RMS amplitude extraction map of the sea floor (Fig. 7) shows lobe-shaped areas characterized by high RMS values on the stoss side of each large-wavelength bedform (highlighted in orange in the grey-scale version of the RMS map in Fig. 7C). In detail, high RMS values can be found where SB1a, SB1b and SB2 fields develop (named Lobe A, Lobe B and Lobe D, respectively, Figs. 6, 7), on the stoss side of LB2 (Lobe C, Figs. 6, 7), of LB4 (Lobe E, Figs. 6, 7), and of LB3 towards the northern flank of channel C-3 (Lobe F in Figs. 6, 7). High RMS amplitude values also characterize the southern flank of C-2, while low values can be detected along the lee side of all the large-wavelength bedforms (Fig. 7).

4.2. Seismic stratigraphy

The stratigraphy of the study area, and in particular of the lobe-shaped features identified in the RMS attribute map (Fig. 7), has been revealed using a combination of 2D arbitrary lines extracted from the 3D seismic cube, surface maps of key stratigraphic horizons and thickness maps (Figs. 8, 9).

Horizon H1, identified by a continuous positive reflection, is the first continuous horizon visible below the sea floor, which can be traced in much of the study area (Figs. 8, 9B). The horizon forms at the base of a series of lobe-to-lens-shaped deposits (named Lobe A to Lobe F, in Figs. 7, 8, 9), whose tops correspond to the sea floor and show high RMS amplitude values. In the same position, corresponding to the stoss side of the large-wavelength bedforms (Figs. 3, 7), the surface map of H1 shows a series of topographic depressions, triangular to circular in shape, with progressively reducing size downslope (Fig. 9B). The thickness map of the unit between the sea floor and horizon H1 (Fig. 9D) shows a series of sediment depocenters up to 65 m thick (Lobe A, Fig. 9D), whose internal seismic character is highlighted in Figure 8 (Lobes A, B, D and F, as examples). Each lobe shows a positive relief with respect to the adjacent sea floor, and is confined basinward by the topography generated by the large-wavelength bedforms (Fig. 8). Lobe A, in detail, is the largest sediment depocenter, covering a surface area of ca. 3.5 km^2 (Fig. 9D), and is composed of thick, high-amplitude, and wavy reflections (seismic lines 1, 2 and 5 in Fig. 8). The sea floor reflection on top of Lobe A is also wavy (Fig. 8), and corresponds to the short-wavelength bedform field SB1a visible on the sea floor maps of Figures 3 and 6. The thickness map (Fig. 9D) highlights that Lobe A is made up of two bodies, with the shallower backstepping with respect to the deeper (see seismic line 5 in Fig. 8). Lobe A accumulates on the stoss side of the large-wavelength bedform LB1, which is confined by horizon H1 at its top and horizon H2 at its base (Figs. 8, 9E).

Horizon H2 shows an erosional character, as highlighted by several truncated reflections (see the black arrows in Fig. 8), and can be traced over part of the study area (Fig. 9C). The topographic depression generated by H2 is exploited by the accumulation of LB1, which is a 90 m thick, L-shaped sediment body (Fig. 9E), made up of continuous, low amplitude reflections, showing a lateral (see seismic lines 3 and 4 in Fig. 8) and upslope direction of migration (see seismic line 5 in Fig. 8), and internal erosional surfaces (highlighted by black dashed lines in the seismic profiles of Figs. 8 and 9). The deposition of the large-wavelength bedform LB1 visible on the sea floor (Figs. 3, 4) creates the accommodation for the accumulation of Lobe A and its downslope confinement, as shown by Figure 9F. Similar geometric relations are observed for each Lobe B to F, where the deposition of a lower unit bounded by an erosional surface (see the red dashed lines in seismic lines 6 and 7 in Fig. 8, and line 8 in Fig. 9) causes the generation of the large-wavelength bedforms and for the formation of accommodation along the slope. Furthermore, RMS amplitude extraction of the sea floor integrated with the seismic facies in cross section highlight that each lobe has high RMS values and is made up by high-amplitude reflections (Fig. 7). By contrast, the units beneath, which crop out on the seafloor along the lee side of the large-wavelength bedforms, present low RMS amplitude and mainly low amplitude seismic reflections (Figs. 7, 8, 9). Consequently, we can infer that the lobes are made of coarser-grained (probably sandy) sediment compared to the deposit beneath that are responsible for the formation of the large-wavelength bedforms, which are probably muddier. The relation between high (low) RMS amplitude values and the presence of coarse-(fine-) grained facies has been described in other contexts, such as submarine channels and mass transport deposits (Posamentier and Kolla, 2003; Moscardelli et al., 2006; Omosanya and Alves, 2013). Correlation of horizon H2 with the other erosional surfaces occurring farther downslope is not straightforward, which poses a problem to the development of a conceptual model explaining their evolution. In the supplementary material, we present two scenarios which take into account the effect of the different processes that might have contributed to the shaping of the sea floor.

5. Discussion

Topographically complex slopes (*sensu* Smith, 2004) occur when tectonic processes or deformation of the sea floor driven by sediment loading on a mobile substrate crate topographic lows or highs that can affect the path and behavior of gravity-driven flows traveling downslope. In such contexts, different types of accommodation may exist (namely ponded and healed slope accommodation; Prather et al., 1998), whose infill reflects the effect of changing accommodation through time (due to deposition) on the behavior of gravity flows, and on the instability of the slope (Prather, 2003). Accommodation can be generated *a-priori*, and then filled by sediments, or can be increased by sediment loading during basin infill, as in the case of salt withdrawal intra-slope basins (Winker, 1996; Prather et al., 1998). It has been demonstrated also that sediment compaction may significantly increase slope accommodation (Reynolds et al., 1991).

As sediment suspension in turbulent flows depends on bed shear stress, which is directly related to flow velocity, 3D sea floor topography may control sediment deposition, erosion or bypass through flow non-uniformity (Kneller and McCaffrey, 1995). Sea floor bedforms in unconfined settings, normally generated by both erosional or depositional turbidity flows and bottom currents (Rebesco et al., 2014; Symons et al., 2016 and references therein), may create relative topographic lows (i.e., the convex-up stoss side of the bedform) where the sediment transported by newly generated gravity flows may accumulate. Such lows can be up to 10^2 m height and 10^3 m long, an order of magnitude smaller in both dimensions than the intra-slope basins of the Gulf of Mexico, and may generate what here we call *stoss-side* *accommodation*. In the study area, deposition from unconfined turbidity flows or bottom currents was probably responsible for the creation of stoss-side accommodation through the deposition of the large-wavelength bedforms (LB1 to LB4 in Fig. 3; see supplementary material).

The ability of a turbidity current to flow across a topographically complex slope, such as a salt withdrawal mini-basin or a large-wavelength bedform, depends on the grain size and flow type (surging vs continuous; Lamb et al., 2004), flow thickness (Lane-Serff et al., 1995), densimetric Froude number and flow stratification (Kneller and McCaffrey, 1999). Complete ponding occurs if the entire flow is trapped within the topographic depression (Patacci et al., 2015, and references therein), and sedimentation farther downslope is expected after its filling, partial or total, through a process called fill-and-spill (Prather et al., 1998). If the depression is small enough compared to the flow, the turbidity current may be able to surmount its downstream lip: the coarse-grained part of the flow will accumulate within the topographic low while the fine-grained cloud will be able to escape through a process called flow stripping (Piper and Normark, 1983; Toniolo et al., 2006).

Experimental results of Lane-Serff et al. (1995) demonstrated that a volume-limited flow (i.e., a surge-like turbidity current) may surmount topographic relief up to 5 times the flow thickness, and that overspill is controlled by the densimetric Froude number of the flow and the ratio between the flow thickness and the obstacle height. Considering a flow whose thickness equals the maximum depth of channel C-A (60 m), and the height of LB1 (the "obstacle", ca. 150 meters), the flow will be always ponded for densimetric $Fr < 1$, and able to overspill only for supercritical flows. Of course this is an approximation based on the results of Lane-Serff et al. (1995), as the vertical density and velocity profiles are also key in determining the maximum run-up height of a turbidity current (Kneller and McCaffrey, 1999; Kneller and Buckee, 2000, and references therein), but in such scenarios stoss-side accommodation will be mainly exploited by deposition of the coarser part of the flow, potentially creating sandy ponded lobes, while the fine-grained cloud of the turbidity current will be likely to overspill. Flow overspill may affect sediment deposition farther downslope, with the potential for development of new sediment corridors. Although with some limitations due to the lack of vertical resolution of the seismic data, this conclusion is supported by the results of this study, which show high RMS amplitude values, considered a proxy for coarse-grained sediment, on the stoss side of each large-wavelength bedform (Fig. 7), and the presence of small channel incisions (named gutter-like channels) mainly along their lee sides, which control deposition basinwards. In addition, the short-wavelength bedforms on Lobe A (Figs. 3, 5) show crest directions perpendicular to the local slope, probably reflecting deposition from turbidity currents radially spreading at the mouth of channel C-A, on the flat surface generated after the infill of the stoss side of LB1. Similar features have been observed in other contexts and linked to deposition from supercritical turbidity currents (Normandeau et al., 2015).

Bottom-hugging sediment-laden flows are highly sensitive to changes in sea floor topography (Casalbore et al., 2018), as divergence or convergence of the streamlines produces sediment deposition or erosion/bypass, respectively (Kneller and McCaffrey, 1995). As in the case of supra-MTD topography (Kneller et al., 2016), pre-existing bedforms may create a complex sea floor topography that will undoubtedly have an effect on such flows, generating sediment deposition, erosion, or bypass, depending on the flow properties and direction with respect to the available stoss-side accommodation. Further work is needed to evaluate the flow behavior across large-wavelength bedforms and for turbidity currents unrelated to the deposition of the bedforms themselves, to quantify the facies association of the ponded lobes through direct sediment sampling, and their preservation potential. This may help to define the role of stoss-side accommodation in hydrocarbon exploration and in the whole evolution of deep-water depositional systems.

6. Conclusion

Sea floor topography is a first order control on the behavior of bottom-hugging sediment-laden flows such as turbidity currents, or of bottom currents. Intra-slope basins are normally associated with large-scale deformation of the sea floor, mainly promoted by salt or gravitational tectonics. With an example from offshore Brazil, we show that topographic variations of the sea floor associated with large-wavelength bedforms (length up to 10^3, and height up to 10^2) may have a substantial effect on subsequent turbidity currents, and may promote the formation of small-scale ponded lobes along the slope. In detail, bedforms characterized by convex-up stoss sides form topographic lows with respect to the adjacent sea floor, generating stoss-side accommodation. Depending on the flow characteristics of newly-sourced turbidity currents with respect to the height of the bedforms, flow stripping or fill-and-spill may occur, in the first case promoting the formation of coarse-grained lobes. The presence of 3D topography may lead to the capture the coarse-grained fractions of the flows in the relative lows while promoting the delivery of only the fine-grained part downstream. Further studies are necessary to fully understand the behavior of sediment-laden flows on complex sea floor topography generated by large-wavelength bedforms, the preservation potential of the ponded deposits, and the role of stoss-side accommodation in the evolution of deep-water depositional systems.

Acknowledgments

We sincerely thank Petroleum Geo-Services (PGS) Investigação Petrolífera Limitada, and specifically David Hajovsky and Scott Opdyke, that kindly provided the dataset and allowed us to show these results. We would also like to thank Schlumberger for providing academic licenses of their software (Petrel). We are grateful to Associate Editor Kei Ogata for his support, and we sincerely thank reviewers Daniele Casalbore and Kamaldeen Omosanya for their comments and suggestions that significantly improved the quality of the manuscript.

Figure captions

Figure 1

Top: Digital elevation model of the Equatorial Atlantic margin (data from GEBCO). Centre: close-up on the Potiguar Basin, offshore Brazil; white rectangle represents the full 3D seismic data coverage, while the study area is highlighted in red; black and orange lines mark the position of the bathymetric profiles presented below. Bottom: bathymetric profiles across the Ceará Plateau (black) and across an open slope setting (orange).

Figure 2

Top: Bathymetric map with 75 m spaced contour lines; NW-SE white lines are the bathymetric profiles presented below, while the thick and continuous red line marks the study area. Note the two large canyon systems bordering the study area (named C-1 and C-3) and the narrower incisional channel (named C-2). The thin dashed red line marks the slope break at the mouth of incisions C-A and C-B. Bottom: Bathymetric profiles across sections AB, CD, EF and GH; note the position of the slope break in sections AB and CD.

Figure 3

A: Bathymetric map of the study area with 75 m spaced contour lines; the white dashed lines mark the crest of the large-wavelength bedforms, named LB1 to LB4; the red dashed line marks the slope break at the mouth of C-A and C-B; the white continuous line marks the position of the bathymetric profile IJ (presented in C). B: Variance attribute map extracted from the sea floor horizon; note the short-wavelength bedforms (SB1a, SB1b, SB2). C: Black line is the bathymetric profile IJ showing the large- and short-wavelength bedforms (grey rectangles), while the red line is the sea floor gradient along the section IJ, with highlighted the different bedform fields.

Figure 4

Variance attribute extracted from the sea floor horizon and presented in a 3D view. The white dashed lines mark the crest of the large-wavelength bedforms (LB1 to LB4), while the red dashed line marks the slope break at the mouth of C-A and C-B. Note the gutter-like channels (Gc) and the short-wavelength bedform SB2.

Figure 5

Wavelength (in km) and height (m) of the different bedform fields recognized in this study. The inset square is a zoom of the lower left corner of the diagram to highlight bedforms SB1a, SB1b and SB2.

Figure 6

Plan view of the sea floor slope map (left) and a close-up 3D of the stoss side of LB1 (right); the red dashed line marks the slope break at the mouth of C-A and C-B; blue squares 1 and 2 highlight short-wavelength bedform fields SB1a and SB2 (zoom visible below), while the red square is an example of seismic artefact. Bathymetric profiles across section ab and cd show bedform styles on SB1, while profile ef shows the bedforms on SB2 (bedform's crests pointed by arrows). Profile gf highlights the seismic artefacts, almost invisible on a bathymetric profile. All the bathymetric profiles are presented at the same scale.

Figure 7

A: Plan view of the RMS attribute map extracted from the sea floor horizon; the white dashed lines mark the crest of the large-wavelength bedforms (LB1 to LB4), while the red dashed line marks the slope break. B: RMS amplitude map presented on an oblique 3D view. Note that the stoss sides of the bedforms are repeatedly characterized by high RMS amplitude values (named Lobe A to Lobe F), and the lee sides by lower values. Note the gutter-like channels (Gc). C: Grey-scale version of the RMS attribute map presented in A. This graphic solution is used to underline the sea floor features: lobes shown with orange overlay, crests of the large-wavelength bedforms in dashed white line, slope break in dashed red line.

Figure 8

2D arbitrary lines (see inset map for location) extracted from the 3D seismic cube, all presented at the same scale. Lines 1 to 5 show Lobes A and B, and the internal stratigraphy of the large-wavelength bedform LB1; seismic lines 6 and 7 show Lobe D and F, respectively. Horizon H2, highlighted in red (note the truncated reflections in sections 4 and 5, for example), marks the base of LB1. Internal reflections of LB1 are continuous and low-amplitude (internal erosional surfaces marked by black dashed lines), and present an oblique to upslope direction of migration as seen on the 3D data. Horizon H1, in black, can be traced at the base of the all the lobes. Note the short-wavelength bedform fields on the sea floor reflection. Red dashed lines on seismic lines 6 and 7 highlight the erosional surface at the base of LB3 and LB4, in analogy with horizon H2.

Figure 9

Top: Seismic line across the large-wavelength bedforms LB1 to LB4, with horizon H2 (continuous red line), horizon H1 (black line), and other erosional surfaces (red dashed lines); see trackline in A. Horizon H1 can be traced in much of the study area and forms the base of the ponded Lobes A to F. A: Sea floor bathymetry. B: Structural map of horizon H1. C: Structural map of horizon H2, at the base of LB1. D: Thickness map generated by the difference between the sea floor and horizon H1, which highlights the ponded Lobes A to F. E: Thickness map generated by the difference between H1 and H2 horizons, which highlights the large-wavelength bedform LB1. F: Combined thickness maps showing how Lobe A is confined basinward by LB1and fills the accommodation generated by the stoss side of LB1.

References

Abreu, V., Sullivan, M., Pirmez, C., Mohrig, D., 2003. Lateral accretion packages (LAPs): an important reservoir element in deep-water sinuous channels. Marine and Petroleum Geology 20, 631-648.

Adeogba, A.A, McHargue, T.R., Graham, S.A., 2005. Transient fan architecture and depositional controls from near-surface 3-D seismic data, Niger delta continental slope. AAPG Bulletin 89, 627-643.

Araripe, P.T., Feijó, F.J., 1994. Carta estratigráfica da Bacia Potiguar. Boletim De Geociências Da Petrobras 8, 127-141.

Armitage, D.A., Romans, B.W., Covault, J.A., Graham, S.A., 2009. The influence of mass-transport-deposit surface topography on the evolution of turbidite architecture: The Sierra Contreras, Tres Pasos Formation (Cretaceous), southern Chile. Journal of Sedimentary Research 79, 287-301.

Badalini, G., Kneller, B., Winker, C.D., 2000. Architecture and processes in the Late Pleistocene Brazos-Trinity turbidite system, Gulf of Mexico Continental Slope. GCSSEPM Foundation 20th Annual Research Conference, Deep-Water Reservoirs of the World, 40-103.

Bahorich, M.S., Farmer, S.L., 1995. 3-D seismic coherency for faults and stratigraphic features. The Leading Edge 14, 1053-1058.

Barton, M.D., 2012. Evolution of an Intra-Slope Apron, Offshore Niger Delta Slope: Impact of Step Geometry on Apron Architecture. In: Prather, B.E., Deptuck, M.E., Mohrig, D., van Hoorn, B., Wynn, R.B., (Eds.), Application of the Principles of Seismic Geomorphology to Continental -Slope and Base-of-Slope Systems: Case Studies from Seafloor and Near-Seafloor Analogues. SEPM Special Publication 99, pp. 181-197.

Beaubouef, R.T., Friedmann, S.J., 2000. High Resolution Seismic/Sequence Stratigraphic Framework for the Evolution of Pleistocene Intra Slope Basins, Western Gulf of Mexico: Depositional Models and Reservoir Analogs. Deep-Water Reservoirs of the World, Gulf Coast SEPM, 40-60.

Berndt, C., Cattaneo, A., Szuman, M., Trincardi, F., Masson, D., 2006. Sedimentary structures offshore Ortona, Adriatic Sea - Deformation or sediment waves? Marine Geology 234, 261-270.

Booth, J.R., Dean, M.C., Duvernay, III, A.E., Styzen, M.J., 2003. Paleo-bathymetric controls on the stratigraphic architecture and reservoir development of confined fans in the Auger Basin: central Gulf of Mexico slope. Marine and Petroleum Geology 20, 563-586.

Brown, A.R., 2004: Interpretation of three-dimensional seismic data, 5th edition. AAPG Memoir 42, Tulsa, Oklahoma, pp. 514.

Casalbore, D., Ridente, D., Bosman, A., Chiocci, F.L., 2017. Depositional and erosional bedforms in Late Pleistocene-Holocene pro-delta deposits of the Gulf of Patti (southern Tyrrhenian margin, Italy). Marine Geology 385, 216-227.

Casalbore, D., Falcini, F., Martorelli, E., Morelli, E., Bosman, A., Calarco, M., Chiocci, F.L. 2018. Characterization of overbanking features on the lower reach of the Gioia-Mesima canyon-channel system (southern Tyrrhenian Sea) through integration of morpho-stratigraphic data and physical modelling. Progress in Oceanography. https://doi.org/10.1016/j.pocean.2018.02.020.

Carter, R.M., 1988. The nature and evolution of deep-sea channel systems. Basin Research 1, 41-54.

Cartigny, M.J.B., Postma, G., van den Berg, J. H., Mastbergen, D.R., 2011. A comparative study of sediment waves and cyclic steps based on geometries, internal structures and numerical modeling. Marine Geology 280, 40-56.

Carvajal, C., Paull, C.K., Caress, D.W., Fildani, A., Lundsten, E., Anderson, K., Maier, K.L., Mcgann, M., Gwiazda, R., Herguera, J.C., 2017. Unraveling the channel-lobe transition zone with high-resolution AUV bathymetry: Navy Fan, Offshore Baja California, Mexico. Journal of Sedimentary Research 87, 1049-1059.

Chen, Q., Sidney, S., 1997. Seismic attribute technology for reservoir forecasting and monitoring. The Leading Edge 16, 445-448.

Condé, V.C., Lana, C.C., Pessoa Neto, O.C., Roesner, E.H., Morais Neto, J.M., Dutra, D.C., 2007. Baciado Ceará. Bol. Geoc. Petrobras 15, 347-355.

Covault, J.A., Kostic, S., Paull, C.K., Ryan, H.F., Fildani, A., 2014. Submarine channel initiation, filling and maintenance from sea-floor geomorphology and morphodynamic modelling of cyclic steps. Sedimentology 61, 1031-1054.

Covault, J.A., Kostic, S., Paull, C.K., Sylvester, Z., Fildani, A., 2017. Cyclic steps and related supercritical bedforms: Building blocks of deep-water depositional systems, western North America. Marine Geology 393, 4-20.

Dalrymple, R.W., Zaitlin, B.A., Boyd, R., 1992. Estuarine facies models: conceptual basis and stratigraphic implications. Journal of Sedimentary Petrology 62, 1130-1146.

Deptuck, M.E., Sylvester, Z., O'Byrne, C.J., 2012. Pleistocene seascape evolution above a "simple" stepped slope-western Niger Delta. In: Prather, B.E., Deptuck, M.E., Mohrig, D., van Hoorn, B., Wynn, R.B., (Eds.), Application of the Principles of Seismic Geomorphology to Continental -Slope and Base-of-Slope Systems: Case Studies from Seafloor and Near-Seafloor Analogues. SEPM Special Publication 99, pp. 199-222.

Ferry, J.N., Mulder, T., Parize, O., Raillard, S., 2005. Concept of equilibrium profile in deep-water turbidite system: effects of local physiographic changes on the nature of sedimentary process and the geometries of deposits. In: Hodgson, D.M., Flint, S.S., (Eds.), Submarine Slope Systems: Processes and Products, Geological Society of London, Special Publications 244, pp. 181-193.

Fildani, A., Normark, W.R., Kostic, S., Parker, G., 2006. Channel formation by flow stripping: large-scale scour features along the Monterey East Channel and their relation to sediment waves. Sedimentology 53, 1265-1287.

Fildani, A., Hubbard, S.M., Covault, J.A., Maier, K.L., Romans, B.W., Traer, M., Rowland, J.C., 2013. Erosion at inception of deep-sea channels. Marine and Petroleum Geology 41, 48-61.

Hawie, N., Covault, J.A., Dunlap, D., Sylvester, Z., 2018. Slope-fan depositional architecture from high-resolution forward stratigraphic models. Marine and Petroleum Geology 91, 576-585.

Heiniö, P., Davies, R.J., 2007. Knickpoint migration in submarine channels in response to fold growth, western Niger Delta. Marine and Petroleum Geology 24, 434-449.

Hughes Clarke, J.E., 2016. First wide-angle view of channelized turbidity currents links migrating cyclic steps to flow characteristics. Nature Communications 7, 1-13.

Jervey, MT., 1988. Quantitative geological modeling of siliciclastic rock sequences and their seismic expression. In: Wilgus, C.K., Hasting, B.S., Kendall, C.G.S.C., Posamentier, H.W., Ross, C.A., Van Wagoner, J., (Eds.), Sea-level Changes-an Integrated Approach, 42, SEPM Special Publication, pp. 47-69.

Jobe, Z.R., Sylvester, Z., Parker, A.O., Howes, N., Slowey, N., Pirmez, C., 2015. Rapid adjustment of submarine channel architecture to changes in sediment supply. Journal of Sedimentary Research 85, 729-753.

Jobe, Z.R., Sylvester, Z., Howes, N., Pirmez, C., Parker, A.O., Cantelli, A., 2017. High-resolution, millennial-scale patterns of bed compensation on a sand-rich intraslope submarine fan, western Niger Delta slope. Geol. Soc. Am. Bull. 129, 23-37.

Jovane, L., Figueiredo, J.J.P., Alves, D.V.P., Iacopini, D., Giorgioni, M., Vannucchi, P., Moura, D.S., Bezerra, F.H.R., Vital, H., Rios, I.L.A., Molina, E.C., 2016. Seismostratigraphy of the Ceará Plateau: Clues to Decipher the Cenozoic Evolution of Brazilian Equatorial Margin. Frontiers in Earth Science doi:10.3389/feart.2016.00090.

Kneller, B., McCaffrey, W.D., 1995. Modelling the effects of salt-induced topography on deposition from turbidity currents. GCSSEPM Foundation 16th Annual Research Conference Salt, Sediment and Hydrocarbons, 137-145.

Kneller, B., McCaffrey, W.D., 1999. Depositional effects of flow nonuniformity and stratification within turbidity currents approaching a bounding slope: deflection, reflection, and facies variation. Journal of Sedimentary Research 69, 980-991.

Kneller, B., Buckee, C., 2000. The structure and fluid mechanics of turbidity currents: a review of some recent studies and their geological implications. Sedimentology, 47, 62-94.

Kneller, B., 2003. The influence of flow parameters on turbidite slope channel architecture. Marine and Petroleum Geology 20, 901-910.

Kneller, B., Dykstra, M., Fairweather, L., Milana, J.P., 2016. Mass-transport and slope accommodation: Implications for turbidite sandstone reservoirs. AAPG Bulletin 100, 213-235.

Kolla, V., Bandyopadhyay, A., Gupta, P., Mukherjee, B., Ramana, D.V., 2012. Morphology and internal structure of a recent upper Bengal fan-valley complex. In: Prather, B.E., Deptuck, M.E., Mohrig, D., Van Horn, B., Wynn, R.B., (Eds.), Application of the Principles of Seismic Geomorphology to Continental-Slope and Base-of-Slope Systems: Case Studies from Seafloor and Near-Seafloor Analogues, SEPM, Special Publication 99, pp. 347-369.

Kostic, S., Casalbore, D., Chiocci, F., Lang, J., Winsemann, J., 2019. Role of Upper-Flow-Regime Bedforms Emplaced by Sediment Gravity Flows in the Evolution of Deltas. Journal of Marine Science and Engineering 7, 5.

Lamb, M.P., Hickson, J.G., Marr, B., Sheets, B., Paola, C., Parker, G., 2004. Surging and continuous turbidity currents: Flow dynamics and deposits in an experimental intraslope minibasin. Journal of Sedimentary Research 74, 148-155.

Lane-Serff, G.F., Beal, L.M., Hadfield, T.D., 1995. Gravity current flow over obstacles. Journal of Fluid Mechanics 292, 39-53.

Matos, R.M.D., 2000. Tectonic evolution of the Equatorial South Atlantic. In: Mohriak, W.U., Talwani, M.. (Eds.), Atlantic Rifts and continental margins, Geophysical Monograph, 115, American Geophysical Union, pp. 332-354.

McHargue, T., Pyrcz, M.J., Sullivan, M.D., Clark, J.D., Fildani, A., Romans, B.W., Covault, J.A., Levy, M., Posamentier, H.W., Drinkwater, N.J., 2011. Architecture of turbidite channel systems on the continental slope: Patterns and predictions. Marine and Petroleum Geology 28, 728-743.

Moscardelli, L., Wood, L., Mann, P., 2006. Mass-transport complexes and associated processes in the offshore area of Trinidad and Venezuela. AAPG Bulletin 90, 1059-1088.

Moscardelli, L., Wood, L., 2016. Morphometry of mass-transport deposits as a predictive tool. GSA Bulletin 128, 47-80.

Mutti, E., Tinterri, R., Remacha, E., Mavilla, N., Angella, S., Fava, L., 1999. An introduction to the analysis of ancient turbidite basins from an outcrop perspective AAPG Course Note 39, pp. 93.

Normandeau, A., Lajeunesse, P., St-Onge, G., 2015. Submarine canyons and channels in the Lower St. Lawrence Estuary (Eastern Canada): Morphology, classification and recent sediment dynamics. Geomorphology 241, 1-18.

Normandeau, A., Lajeunesse, P., Poiré, A.G., Francus, P., 2016. Morphological expression of bedforms formed by supercritical sediment density flows on four fjord-lake deltas of the south-eastern Canadian Shield (Eastern Canada). Sedimentology 63, 2106-2129.

Normark, W.R., Piper, D.J.W., Posamentier, H., Pirmez, C., Migeon, S., 2002. Variability in form and growth of sediment waves on turbidite channel levees. Marine Geology 192, 23-58.

Omosanya, K.O., Alves, T.M., 2013. A 3-dimensional seismic method to assess the provenance of Mass-Transport Deposits (MTDs) on salt-rich continental slopes (Espírito Santo Basin, SE Brazil). Marine and Petroleum Geology 44, 223-239.

Paull, C.K., Ussler III, W., Caress, D.W., Lundsten, E., Covault, J.A., Maier, K.L., Xu, J., Augenstein, S., 2010. Origins of large crescent-shaped bedforms within the axial channel of Monterey Canyon, offshore California. Geosphere 6, 755-774.

Paull, C.K., Caress, D.W., Ussler III, W., Lundsten, E., Meiner-Johnson, M., 2011. High-resolution bathymetry of the axial channels within Monterey and Soquel submarine canyons, offshore central California. Geophere 7, 1077-1101.

Patacci, M., Haughton, P.D.W., McCaffrey, W.D., 2015. Flow behavior of ponded turbidity currents. Journal of Sedimentary Research 85, 885-902.

Piper, D.J.W., Normark, W.R., 1983. Turbidite depositional patterns and flow characteristics, Navy submarine fan, California Borderland. Sedimentology 30, 681-694.

Piper, D.J.W., Normark, W.R., 2009. Processes that initiate turbidity currents and their influence on turbidites: a marine geology perspective. Journal of Sedimentary Research 79, 347-362.

Pirmez, C., Beauboeuf, R.T., Friedmann, S.J., Mohrig, D.C., 2000. Equilibrium profile and baselevel in submarine channels: examples from Late Pleistocene systems and implications for the architecture of deepwater reservoirs. In: Weimer, P., Slatt, R.M., Coleman, J., Rosen, N.C., Nelson, H., Bouma, A.H., Styzen, M.J., Lawrence, D.T., (Eds.), Deep water reservoirs of the world, GCSSEPM Foundation, Houston, pp. 782-805.

Prather, B.E., Booth, J.E., Steffens, G.S., Craig, P.A., 1998. Classification, lithologic calibration, and stratigraphic succession of seismic facies of intraslope basins, deep-water Gulf of Mexico. AAPG Bulletin 82, 701-728.

Prather, B.E., 2003. Controls on reservoir distribution, architecture and stratigraphic trapping in slope settings. Marine and Petroleum Geology 20, 529-545.

Prather, B.E., Pirmez, C., Winker, C.D., 2012. Stratigraphy of linked intraslope basins: Brazos-Trinity system Western Gulf of Mexico. In: Prather, B.E., Deptuck, M.E., Mohrig, D., van Hoorn, B., Wynn, R.B., (Eds.), Application of the Principles of Seismic Geomorphology to Continental -Slope and Base-of-Slope Systems: Case Studies from Seafloor and Near-Seafloor Analogues. SEPM Special Publication 99, pp. 83-109.

Posamentier, H.W., Kolla, V., 2003. Seismic Geomorphology and Stratigraphy of Depositional Elements in Deep-Water Settings. Journal of Sedimentary Research 73, 367-388.

Rebesco, M., Hernández-Molina, F.J., van Rooij, D., Wåhlin, A., 2014. Contourites and associated sediments controlled by deep-water circulation processes: State of the art and future considerations. Marine Geology 352, 111-154.

Reijenstein, H.M., Posamentier, H.W., Bhattacharya, J.P., 2011. Seismic geomorphology and high-resolution seismic stratigraphy of inner-shelf fluvial, estuarine, deltaic, and marine sequences, Gulf of Thailand. AAPG Bulletin 95, 1959-1990.

Rijks, E.J.H., Jauffred, J.C.E.M., 1991. Seismic interpretation 29; attribute extraction; an important application in any detailed 3-D interpretation study. The Leading Edge 10, 11-19.

Reynolds, D.J., Steckler, M.S., Coakley, B.J., 1991. The role of the sediment load in sequence stratigraphy: The influence of flexural isostasy and compaction. Journal of Geophysical Research B01914.

Sinclair, H.D., Tomasso, M., 2002. Depositional Evolution of Confined Turbidite Basins. Journal of Sedimentary Research 72, 451-456.

Smith, R., 2004. Silled sub-basins to connected tortuous corridors: sediment distribution systems on topographically complex sub-aqueous slopes. Geological Society of London Special Publications 222, 23-43.

Smith, D.P., Kvitek, R., Iampietro, P.J., Wong, K., 2007. Twenty-nine months of geomorphic change in upper Monterey Canyon (2002–2005). Marine Geology 236, 79-94.

Soutter, E.L., Kane, I.A., Huuse, M., 2018. Giant submarine landslide triggered by Paleocene mantle plume activity in the North Atlantic. Geology 46, 511-514.

Symons, W.O., Sumner, E.J., Talling, P.J., Cartigny, M.J.B., Clare, M.A., 2016. Large-scale sediment waves and scours on the modern seafloor and their implications for the prevalence of supercritical flows. Marine Geology 371, 130-148.

Talling, P.J., Allin, J., Armitage, D.A., Arnott, R.W.C., Cartigny, M.J.B., Clare, M.A., Felletti, F., Covault, J.A., Girardclos, S., Hansen, E., Hill, P.R., Hiscott, R.N., Hogg, A.J., Hughes Clarke, J.E., Jobe, Z.R., Malgesini, G., Mozzato, A., Naruse, H., Parkinson, S., Peel, F.J., Piper, D.J.W., Pop, E., Postma, G., Rowley, P., Sguazzini, A., Stevenson, C.J., Sumner, E.J., Sylvester, Z., Watts, C., Xu, J., 2015. Key future directions for research on turbidity currents and their deposits. Journal Sedimentary Research 85, 153-169.

Toniolo, H., Lamb, M.P., Parker, G., 2006. Depositional turbidity currents in diapiric minibasins on the continental slope: Formulation and theory. Journal of Sedimentary Research 76, 783-797.

Vail, PR., 1987. Seismic stratigraphy interpretation using sequence stratigraphy. Part I: Seismic stratigraphy interpretation procedure. In Atlas of Seismic Stratigraphy, ed. AW Bally, pp. 1-10. Am. Assoc. Petrol. Geol. Stud. Geol. No. 27, Vol. 1. 125 pp.

Ward, N.I., Alves, T.M., Blenkinsop, T.G., 2018. Submarine sediment routing over a blocky mass-transport deposit in the Espírito Santo Basin, SE Brazil. Basin Research 30, 816-834.

Winker, C.D., 1996. High-resolution seismic stratigraphy of a late Pleistocene submarine fan ponded by salt-withdrawal mini-basins on the Gulf of Mexico continental slope. 28th Annual Offshore Technology Conference, Proceedings, pp. 619-628.

Wynn, R.B., Stow, D.A.V., 2002. Classification and characterisation of deep-water sediment waves. Marine Geology 192, 7-22.

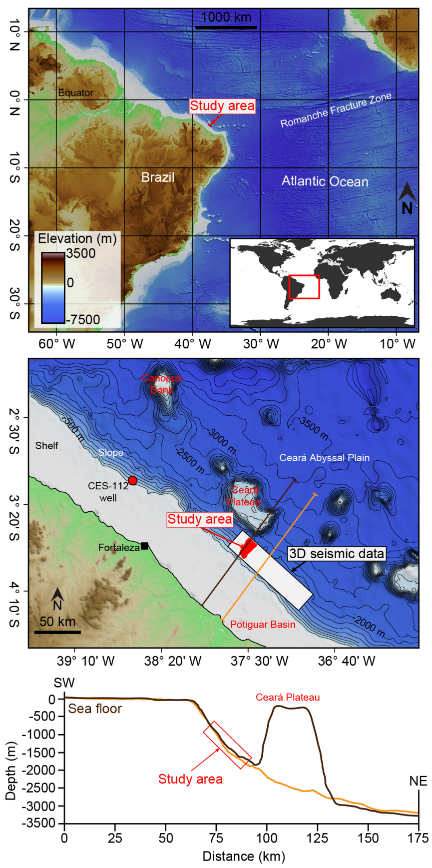

1000 km
10° N
0° N
10° S
20° S
30° S
Equator
Study area
Romanche Fracture Zone
Brazil
Atlantic Ocean
N
Elevation (m)
3500
0
-7500
60° W
50° W
40° W
30° W
20° W
10° W
2° 30' S
3° 20' S
4° 10' S
Shelf
Slope
CES-112 well
Fortaleza
-3000 m
-3500 m
-2500 m
-2000 m
Ceará Abyssal Plain
Ceará Plateau
Study area
3D seismic data
Potiguar Basin
N
50 km
39° 10' W
38° 20' W
37° 30' W
36° 40' W
SW
NE
Sea floor
Ceará Plateau
Study area
Depth (m)
0
-500
-1000
-1500
-2000
-2500
-3000
-3500
0
25
50
75
100
125
150
175
Distance (km)

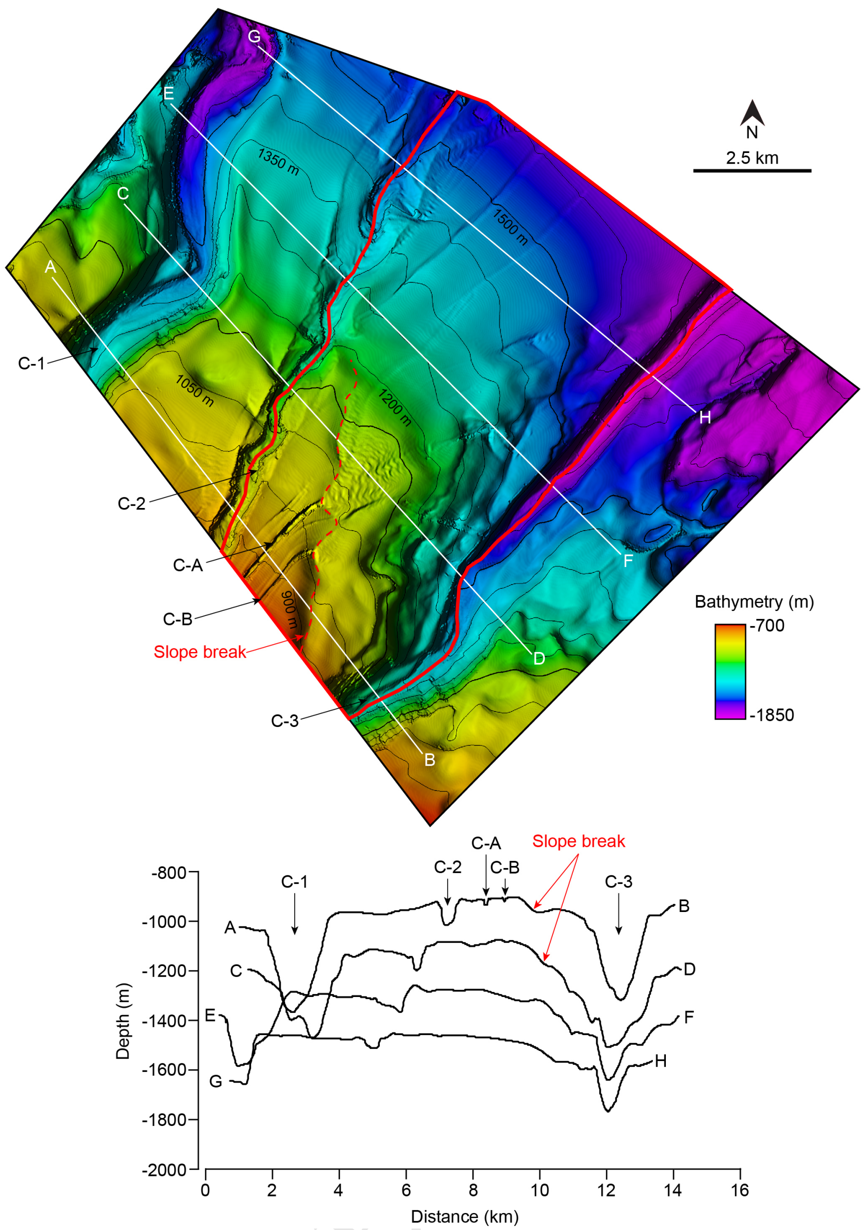

G
E
C
A
1350 m
1500 m
1050 m
1200 m
900 m
N
2.5 km
C-1
C-2
C-A
C-B
Slope break
C-3
H
F
D
B
Bathymetry (m)
-700
-1850
C-A
Slope break
C-2
C-B
C-1
C-3
A
B
C
D
E
F
G
H
Depth (m)
-800
-1000
-1200
-1400
-1600
-1800
-2000
0
2
4
6
8
10
12
14
16
Distance (km)

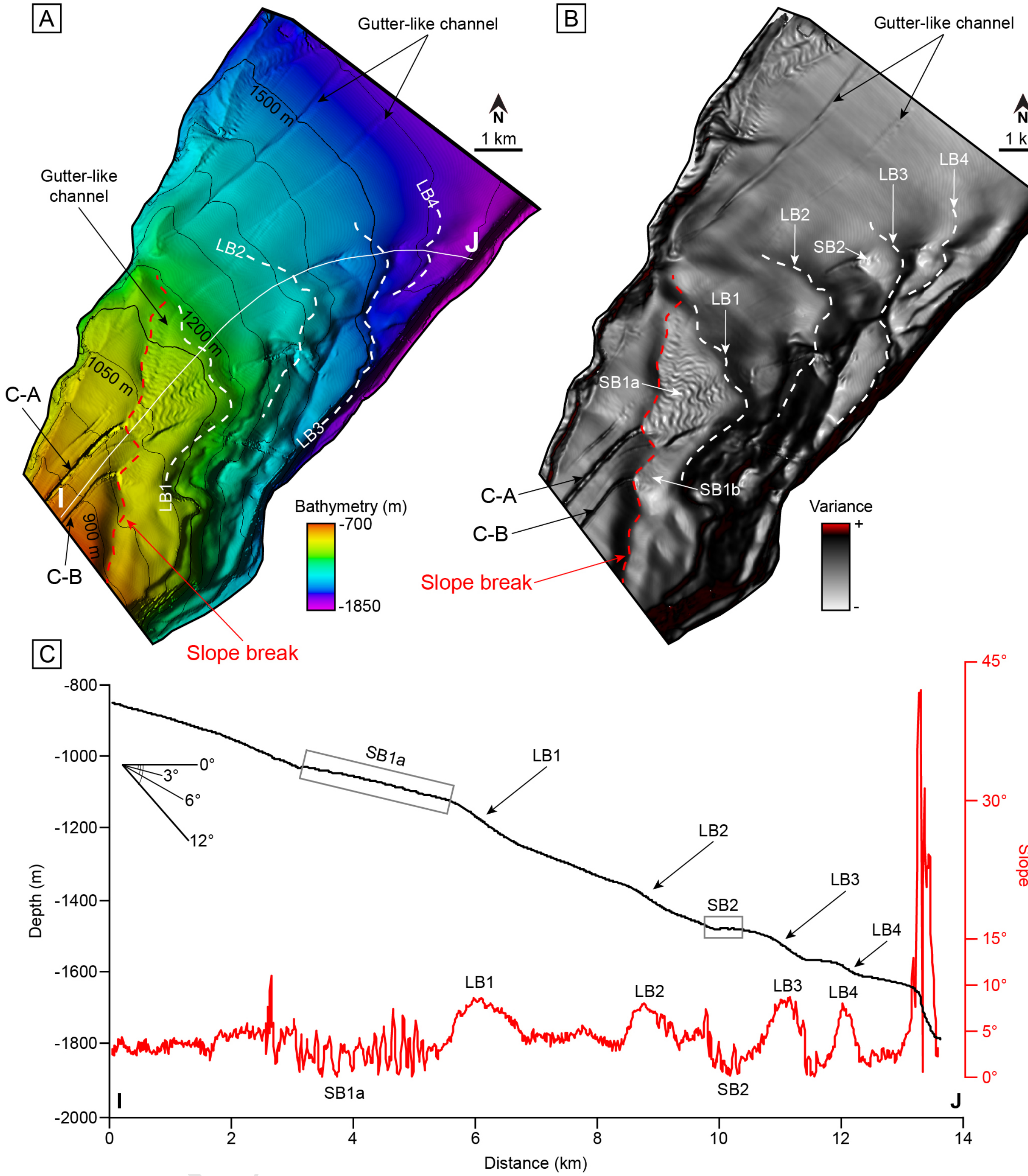

A
Gutter-like channel
Gutter-like channel
1500 m
1200 m
1050 m
900 m
LB1
LB2
LB3
LB4
C-A
C-B
I
J
Slope break
N
1 km
Bathymetry (m)
-700
-1850
B
SB1a
SB1b
SB2
Variance
+
-
C
Depth (m)
Distance (km)
Slope
0°
3°
6°
12°
5°
10°
15°
30°
45°

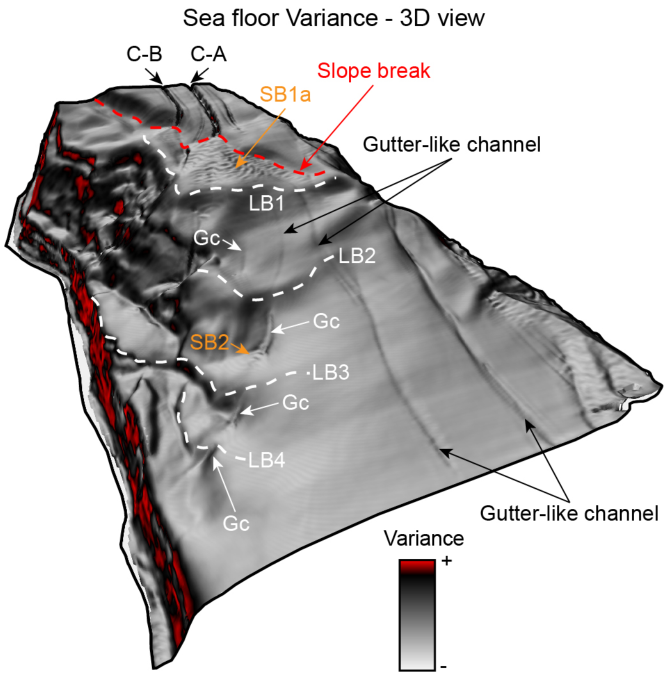

Sea floor Variance - 3D view
C-B
C-A
Slope break
SB1a
Gutter-like channel
LB1
Gc
LB2
Gc
SB2
LB3
Gc
LB4
Gc
Gutter-like channel
Variance
+
-

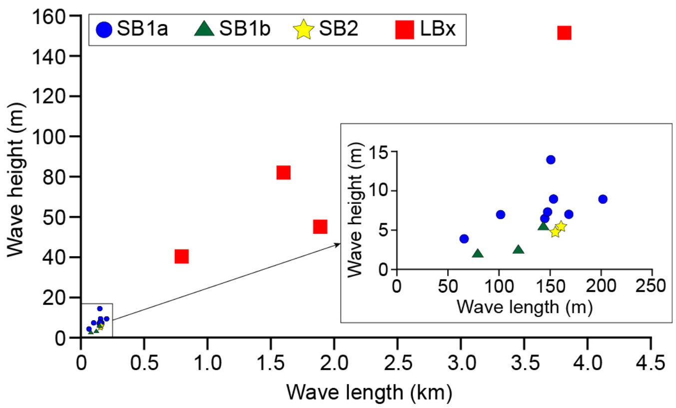
SB1a
SB1b
SB2
LBx
Wave height (m)
Wave length (km)
0
0.5
1.0
1.5
2.0
2.5
3.0
3.5
4.0
4.5
0
20
40
50
80
100
120
140
160
Wave height (m)
Wave length (m)
0
50
100
150
200
250
0
5
10
15

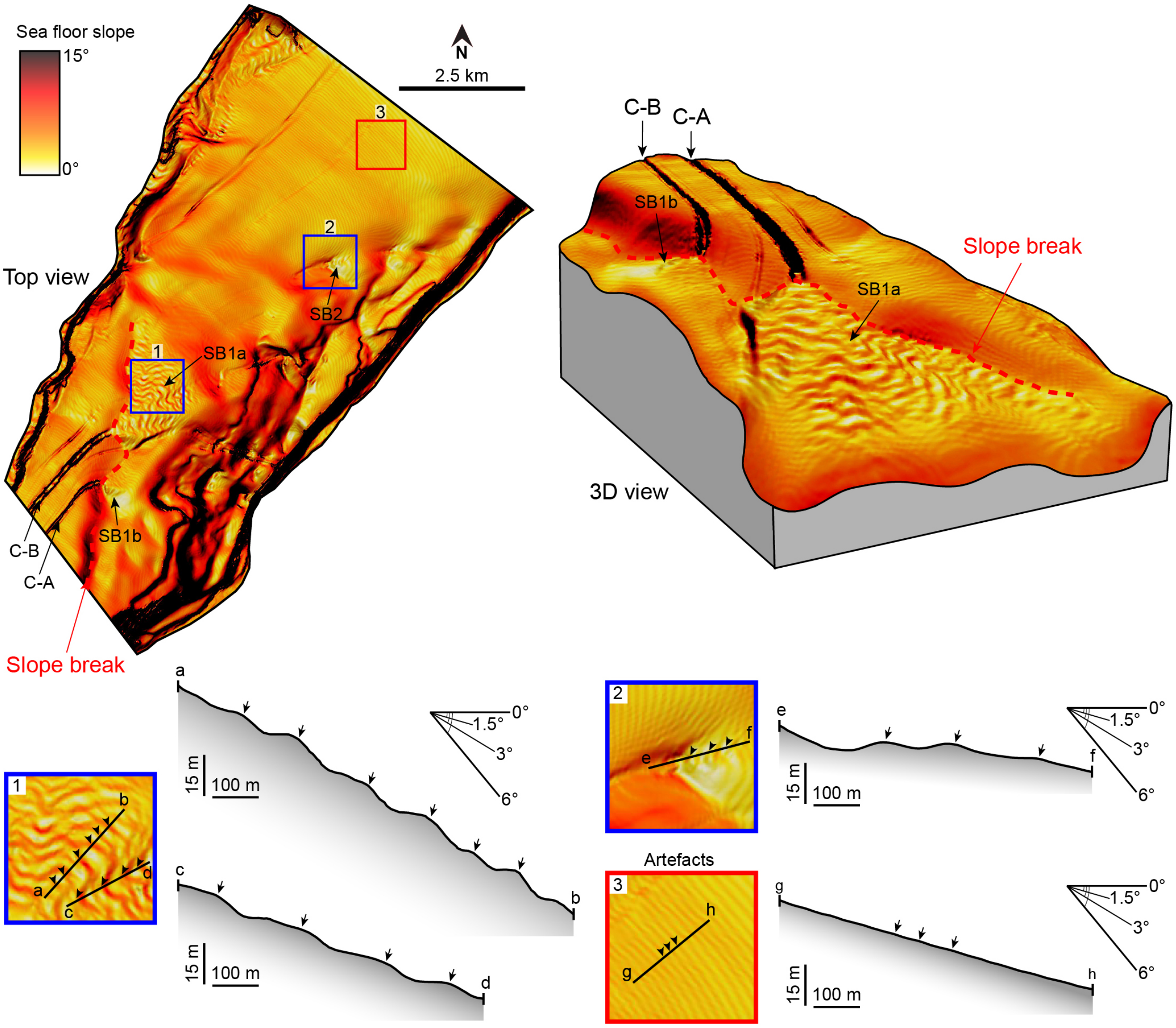
Sea floor slope
15°
0°
2.5 km
N
Top view
3
2
SB2
1
SB1a
SB1b
C-B
C-A
Slope break
C-B
C-A
SB1b
Slope break
SB1a
3D view
a
b
c
d
15 m
100 m
0°
1.5°
3°
6°
2
e
f
Artefacts
3
g
h

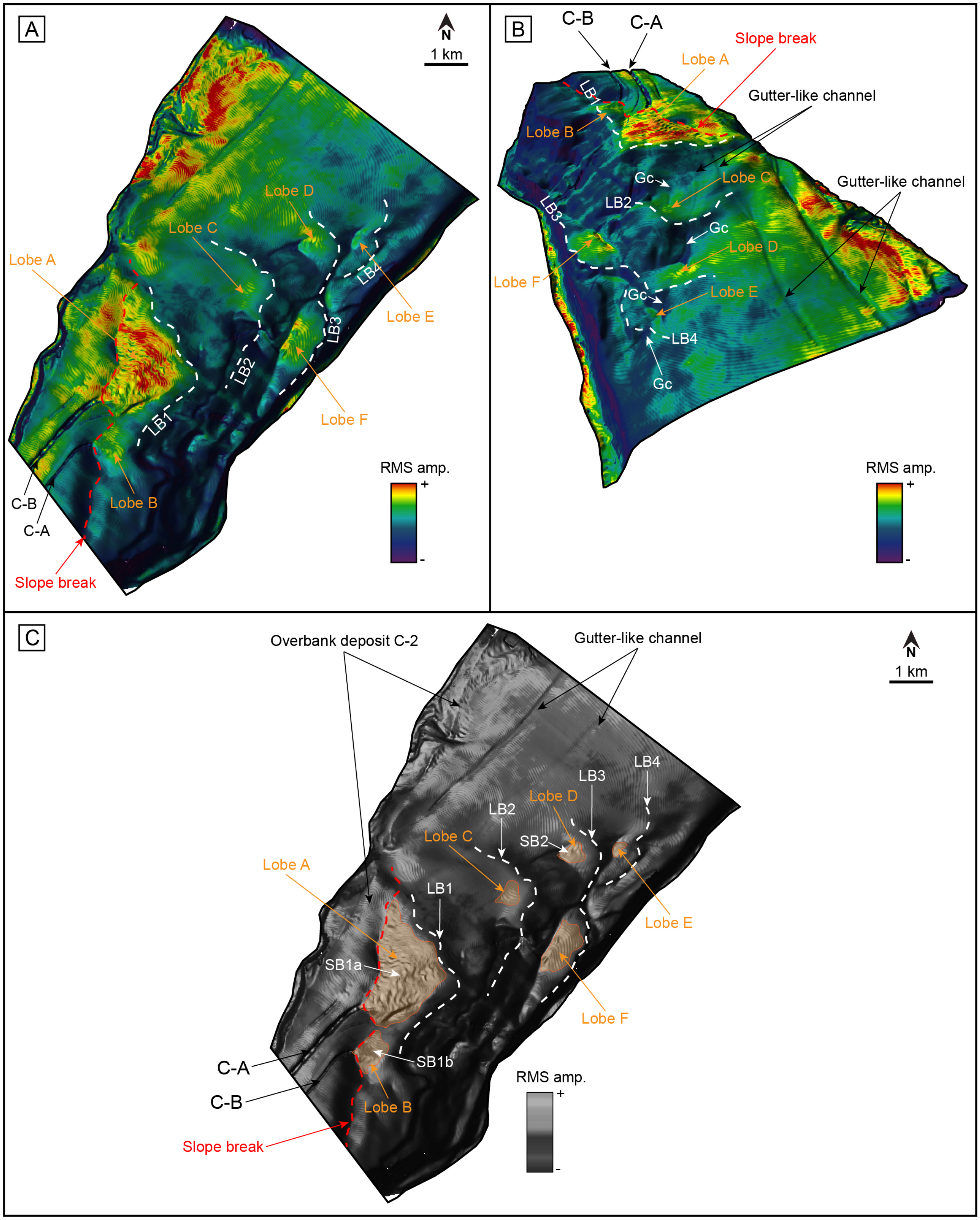
A
1 km
Lobe A
Lobe B
Lobe C
Lobe D
Lobe E
Lobe F
LB1
LB2
LB3
LB4
C-B
C-A
Slope break
RMS amp.
B
C-B
C-A
Slope break
Lobe A
Lobe B
Gutter-like channel
Gc
Lobe C
LB2
Lobe D
Lobe E
Lobe F
LB3
LB4
Gc
C
Overbank deposit C-2
Gutter-like channel
1 km
LB1
LB2
LB3
LB4
SB1a
SB1b
SB2
C-A
C-B
Slope break
RMS amp.

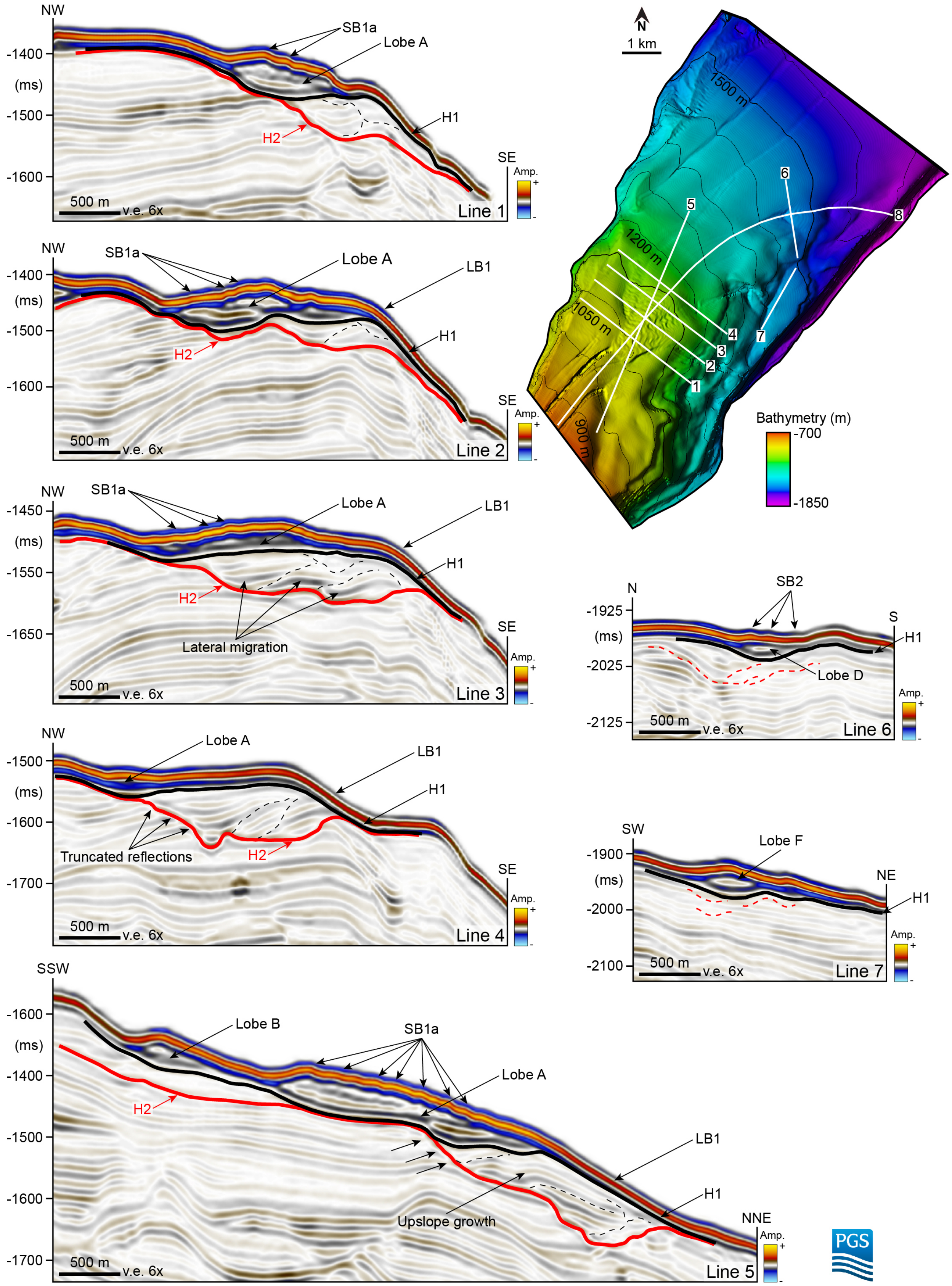
NW
SE
SB1a
Lobe A
H1
H2
Line 1
Line 2
Line 3
Line 4
Line 5
Line 6
Line 7
LB1
Lateral migration
Truncated reflections
Upslope growth
Lobe B
Lobe D
Lobe F
SB2
SSW
NNE
N
S
SW
NE
(ms)
500 m
v.e. 6x
Amp.
N
1 km
1500 m
1200 m
1050 m
900 m
Bathymetry (m)
-700
-1850
PGS

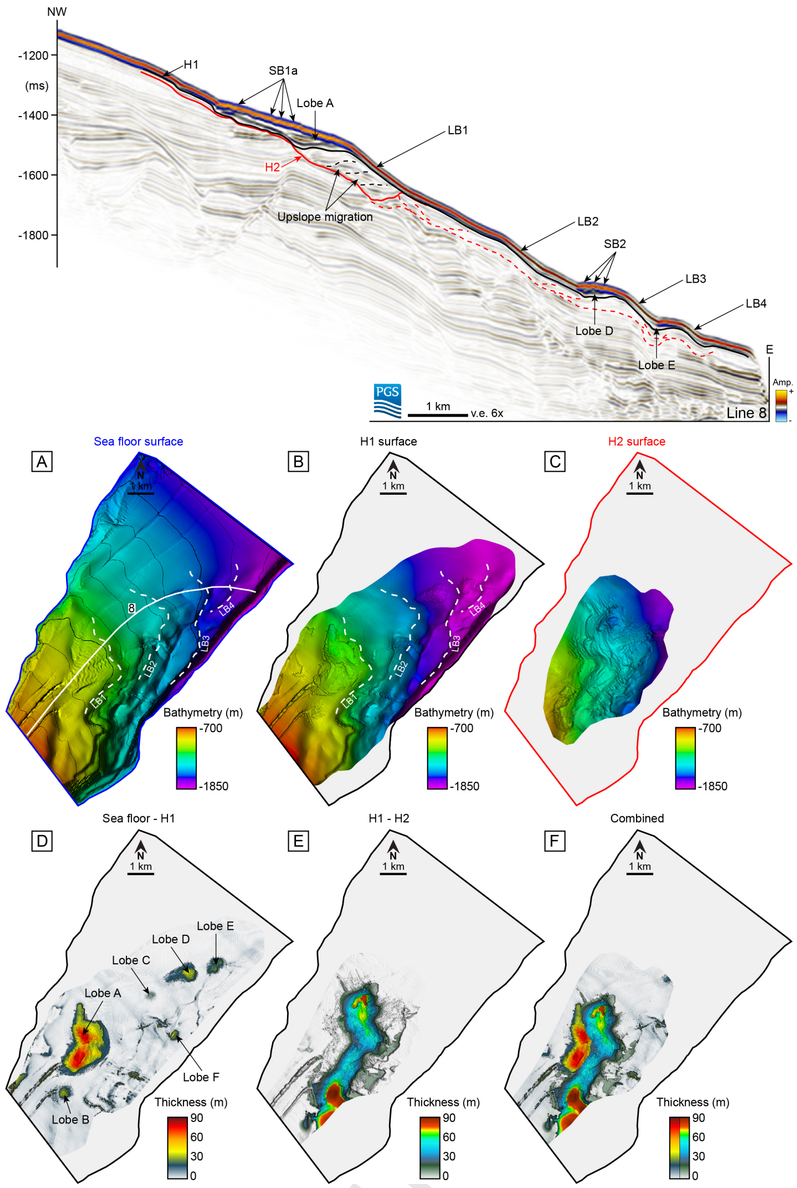
NW
-1200
(ms)
-1400
-1600
-1800
H1
SB1a
Lobe A
LB1
H2
Upslope migration
LB2
SB2
LB3
LB4
Lobe D
Lobe E
E
Amp.
PGS
1 km
v.e. 6x
Line 8
Sea floor surface
H1 surface
H2 surface
A
B
C
Bathymetry (m)
-700
-1850
D
E
F
Sea floor - H1
H1 - H2
Combined
Lobe A
Lobe B
Lobe C
Lobe D
Lobe E
Lobe F
Thickness (m)
90
60
30
0